

B-cos Networks: Alignment is All We Need for Interpretability

Moritz Böhle
MPI for Informatics
Saarland Informatics Campus

Mario Fritz
CISPA Helmholtz Center
for Information Security

Bernt Schiele
MPI for Informatics
Saarland Informatics Campus



Fig. 1. Top: Inputs \mathbf{x}_i to a B-cos DenseNet-121. **Bottom:** B-cos network explanation for class c (c : image label). Specifically, we visualise the c -th row of $\mathbf{W}_{1 \rightarrow L}(\mathbf{x}_i)$ as applied by the model, see Eq. (13); **no masking of the original image is used for these visualisations**. For the last 2 images, we also show the explanation for the 2nd most likely class. For details on the visualisation of $\mathbf{W}_{1 \rightarrow L}(\mathbf{x}_i)$, see Sec. 4.

Abstract

We present a new direction for increasing the interpretability of deep neural networks (DNNs) by promoting weight-input alignment during training. For this, we propose to replace the linear transforms in DNNs by our B-cos transform. As we show, a sequence (network) of such transforms induces a single linear transform that faithfully summarises the full model computations. Moreover, the B-cos transform introduces alignment pressure on the weights during optimisation. As a result, those induced linear transforms become highly interpretable and align with task-relevant features. Importantly, the B-cos transform is designed to be compatible with existing architectures and we show that it can easily be integrated into common models such as VGGs, ResNets, InceptionNets, and DenseNets, whilst maintaining similar performance on ImageNet. The resulting explanations are of high visual quality and perform well under quantitative metrics for interpretability.

Code available at github.com/moboehle/B-cos.

1. Introduction

While deep neural networks (DNNs) are highly successful in a wide range of tasks, explaining their decisions remains an open research problem [30]. The difficulty here lies in the fact that such explanations need to faithfully summarise the internal model computations and present them in a human-interpretable manner. E.g., it is well known that piece-wise linear models (e.g., ReLU-based [25]) are accurately summarised by a linear transform for every input [24]. However, despite providing an accurate summary, these piece-wise linear transforms are gen-

erally not intuitively interpretable for humans and typically perform poorly under quantitative interpretability metrics, cf. [33, 44]. Recent work thus aimed to improve the explanations’ interpretability, often focusing on their visual quality [2]. However, gains in the visual quality of the explanations often came at the cost of their model-faithfulness [2]. Instead of optimising the explanation method, in this work we aim to optimise the DNNs to inherently provide an explanation that fulfills the aforementioned requirements—the resulting explanations constitute both a faithful summary and have a clear interpretation for humans. For this, we propose the **B-cos transform** as a drop-in replacement for linear transforms. As such, the B-cos transform can easily be integrated into a wide range of existing DNN architectures and we show that the resulting B-cos DNNs provide high-quality explanations for their decisions, see Fig. 1.

To ensure that these explanations constitute a faithful summary of the models, we design the B-cos transform as an input-dependent linear transform. Importantly, any sequence of such transforms therefore induces a single linear transform that faithfully summarises the entire sequence. In order to make the induced linear transforms interpretable, the B-cos transform is designed to induce alignment pressure on the weights during optimisation, which optimises the model weights to align with task-relevant input patterns. The linear transform induced by the model thus has a clear interpretation: it is a direct reflection of the weights the model has learnt during training and specifically reflects those weights that best align with a given input.

In summary, we make the following contributions:

- (1) We introduce the B-cos transform to improve neural network interpretability. By promoting weight-input align-

ment, these transforms are explicitly designed to yield explanations that highlight task-relevant patterns in the input.

(2) Specifically, the B-cos transform is designed such that any sequence of B-cos transforms can be faithfully summarised by a single linear transform. We show that this allows to explain not only the models’ output neurons, but also neurons from arbitrary intermediate network layers.

(3) We demonstrate that a plain B-cos convolutional neural network without any additional non-linearities, batch-norm layers [15], or regularisation schemes can achieve competitive performance on CIFAR10 [19]. In an ablation study we also show that the parameter B allows for fine-grained control over the increase in weight alignment and thus the interpretability of the B-cos networks.

(4) To highlight the generality of our approach, we show that the B-cos transform can easily be integrated into various commonly used DNNs such as InceptionNet [40], ResNet [13], VGG [35], and DenseNet [14] models, whilst maintaining similar performance. More importantly, the resulting architectures are highly interpretable under the B-cos explanations and outperform other explanation methods across all tested architectures, both under quantitative metrics as well as under qualitative inspection.

2. Related work

Approaches for understanding DNNs typically focus on explaining individual model decisions *post-hoc*, i.e., they are designed to work on any pre-trained DNN. Examples of this include perturbation-based, [22, 27, 29], activation-based, [8, 17], or backpropagation-based explanations, [3, 31, 33, 34, 36, 37, 39, 45]. In order to obtain explanations for the B-cos networks, we also rely on a backpropagation-based approach. In contrast to post-hoc explanation methods, however, we optimise the B-cos networks to be explainable under this particular form of backpropagation and the resulting explanations are thus model-inherent.

The design of such *inherently interpretable* models has gained increased attention recently. Examples include prototype-based networks [7], BagNets [5], and CoDA Nets [6]. Similar to the BagNets and the CoDA Nets, our B-cos networks can be faithfully summarised by a single linear transform. Moreover, similar to [6], we rely on a structurally induced alignment pressure to make those transforms interpretable. In contrast to those works, however, our method is specifically designed to be compatible with existing neural network architectures, which allows us to improve the interpretability of a wide range of DNNs.

Weight-input alignment in DNNs has recently received increased attention. E.g., it has been observed that adversarial training promotes alignment [41] and recent studies suggest that this could increase interpretability via gradient-based explanations [16, 32]. Further, [38] introduce a loss to in-

crease alignment. Instead of relying on loss-based model regularisation, the increase in alignment in B-cos networks is based on *architectural constraints* that require weight-input alignment for solving the optimisation task.

Non-linear transforms. While the linear transform is the default operation for most neural network architectures, many non-linear transforms have been investigated, [11, 20, 21, 23, 43, 46]. Most similar to our work are [20, 21, 23], which assess transforms that emphasise the cosine similarity (i.e., ‘alignment’) between weights and inputs to improve model performance. In fact, we found that amongst other transforms, [20] evaluates a non-linear transform that is equivalent to our B-cos operator with B=2. In contrast to [20], we explicitly introduce this non-linear transform to increase interpretability and show that such models can be scaled to large-scale classification problems.

3. B-cos neural networks

In this section, we introduce the B-cos transform as a replacement for the linear units in DNNs, which are (almost) “at the heart of every deep network” [28], and discuss how this can increase the interpretability of DNNs.

For this, we first introduce the B-cos transform as a variation of the linear transform in Sec. 3.1 and highlight its most important properties. In Sec. 3.2, we show how to construct B-cos networks and how to faithfully summarise the network computations to obtain explanations for their outputs (3.2.1). Then, we discuss how the B-cos transform—combined with the binary cross entropy (BCE) loss—affects the parameter optima of the models (3.2.2). Specifically, by inducing alignment pressure, the B-cos transform aligns the model weights with task-relevant patterns in the input. Finally, in Sec. 3.3 we integrate the B-cos transform into conventional DNNs by using it as a drop-in replacement for the ubiquitously used linear units.

3.1. The B-cos transform

Typically, the individual ‘neurons’ in a DNN compute the dot product between their weights \mathbf{w} and an input \mathbf{x} :

$$f(\mathbf{x}; \mathbf{w}) = \mathbf{w}^T \mathbf{x} = \|\mathbf{w}\| \|\mathbf{x}\| c(\mathbf{x}, \mathbf{w}), \quad (1)$$

$$\text{with } c(\mathbf{x}, \mathbf{w}) = \cos(\angle(\mathbf{x}, \mathbf{w})). \quad (2)$$

Here, $\angle(\mathbf{x}, \mathbf{w})$ returns the angle between the vectors \mathbf{x} and \mathbf{w} . In this work, we seek to improve the interpretability of DNNs by promoting weight-input alignment during optimisation. To achieve this, we propose the **B-cos transform**:

$$\text{B-cos}(\mathbf{x}; \mathbf{w}) = \underbrace{\|\hat{\mathbf{w}}\|}_{=1} \|\mathbf{x}\| c(\mathbf{x}, \hat{\mathbf{w}})^B \times \text{sgn}(c(\mathbf{x}, \hat{\mathbf{w}})). \quad (3)$$

Here, B is a hyperparameter, the hat-operator scales $\hat{\mathbf{w}}$ to unit norm, and sgn denotes the sign function. Note that this only introduces *minor changes* (highlighted in blue) with

respect to Eq. (1); e.g., note that for $B = 1$, the B-cos transform is equivalent to a linear transform with $\widehat{\mathbf{w}}$. However, albeit small, these changes are important for three reasons. **First**, they bound the output of B-cos neurons, i.e.,

$$\|\widehat{\mathbf{w}}\| = 1 \Rightarrow \text{B-cos}(\mathbf{x}; \mathbf{w}) \leq \|\mathbf{x}\|. \quad (4)$$

As becomes clear from Eq. (D.1), equality in Eq. (4) is only achieved if \mathbf{x} and \mathbf{w} are collinear, i.e., *aligned*.

Secondly, by increasing the exponent B , the output for badly aligned weights can be further suppressed,

$$B \gg 1 \wedge |c(\mathbf{x}, \widehat{\mathbf{w}})| < 1 \Rightarrow \text{B-cos}(\mathbf{x}; \mathbf{w}) \ll \|\mathbf{x}\|, \quad (5)$$

and the respective B-cos unit can only produce outputs close to its maximum (i.e., $\|\mathbf{x}\|$) for a small range of angular deviations from \mathbf{x} . In combination, these two properties can significantly alter the optima of the weight vectors \mathbf{w} . To illustrate this, we show in Fig. 2 how increasing B affects a simple linear classification problem. In particular, Eqs. (4) and (5) shift the optimum of the optimisation problem such that for large B the optimal weights align with the red data cluster, independent of the other class. In contrast to the *discriminative explanation* of a linear classifier, which is highly task-dependent (see, e.g., first row in Fig. 2) the B-cos transform allows for a *similarity-based explanation*: a sample is confidently classified as the red class if it is aligned well with the corresponding weight vector.

Lastly, these changes maintain an important property of the linear transform: similar to sequences of linear transforms, sequences of B-cos transforms can still be faithfully summarised by a single linear transform (Eq. (13)). Given the bound (Eq. (4)) and the suppression of outputs for badly aligned weights (Eq. (5)) these linear transforms will align with discriminative patterns when optimising a B-cos network for classification, see Sec. 3.2.2. As a result, these transforms are well suited to explain the model outputs.

3.2. Simple (convolutional) B-cos networks

In this section, we first discuss how to construct simple (convolutional) DNNs based on the B-cos transform. Then, we show how to summarise the network outputs by a single linear transform and, finally, why this transform aligns with discriminative input patterns in classification tasks.

B-cos networks. The B-cos transform is designed as a drop-in replacement of the linear transform, i.e., it can be used in exactly the same way. For example, first consider a *conventional* fully connected multi-layer neural network $\mathbf{f}(\mathbf{x}; \theta)$ of L layers, represented by

$$\mathbf{f}(\mathbf{x}; \theta) = \mathbf{l}_L \circ \mathbf{l}_{L-1} \circ \dots \circ \mathbf{l}_2 \circ \mathbf{l}_1(\mathbf{x}), \quad (6)$$

with \mathbf{l}_j denoting layer j with parameters \mathbf{w}_j^k for neuron k in layer j , and θ the collection of all model parameters. In

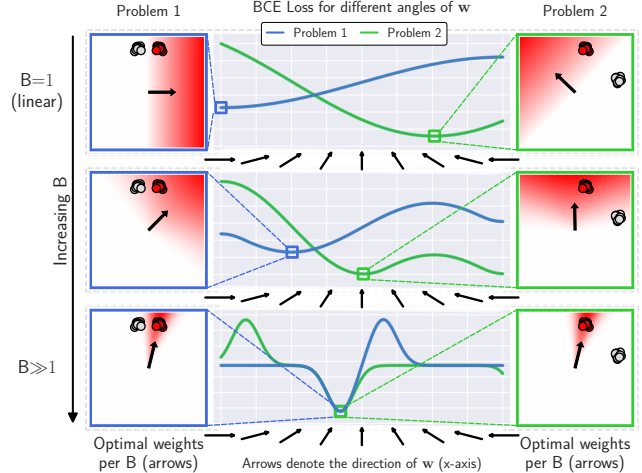


Fig. 2. Col. 2: BCE loss for different angles of \mathbf{w} for B-cos classifiers (Eq. (D.1)) with different values of B (rows) for two classification problems. **Cols. 1+3:** Visualisation of the classification problems and the corresponding optimal weights (arrows) per B . For $B=1$ (first row) the weights \mathbf{w} represent the decision boundary of a linear classifier. Although the red cluster is the same in both cases, the optimal weight vectors differ significantly (compare within row). In contrast, for higher values of B the weights converge to the same optimum in both tasks (see last row).

such a model, each layer \mathbf{l}_j typically computes

$$\mathbf{l}_j(\mathbf{a}_j; \mathbf{W}_j) = \phi(\mathbf{W}_j \mathbf{a}_j), \quad (7)$$

with \mathbf{a}_j the input to layer j , ϕ a non-linear activation function (e.g., ReLU), and the row k of \mathbf{W}_j given by the weight vector \mathbf{w}_j^k of the k -th neuron in that layer. Note that the non-linear activation function ϕ is *required* to be able to model non-linear relationships with multiple layers in sequence.

A corresponding B-cos network \mathbf{f}^* with layers \mathbf{l}_j^* can be formulated in exactly the same way as

$$\mathbf{f}^*(\mathbf{x}; \theta) = \mathbf{l}_L^* \circ \mathbf{l}_{L-1}^* \circ \dots \circ \mathbf{l}_2^* \circ \mathbf{l}_1^*(\mathbf{x}), \quad (8)$$

with the only difference being that every dot product (here between rows of \mathbf{W}_j and the input \mathbf{a}_j) is replaced by the B-cos transform in Eq. (D.1). In matrix form, this equates to

$$\mathbf{l}_j^*(\mathbf{a}_j; \mathbf{W}_j) = |c(\mathbf{a}_j; \widehat{\mathbf{W}}_j)|^{B-1} \times \left(\widehat{\mathbf{W}}_j \mathbf{a}_j \right). \quad (9)$$

Here, the power, absolute value, and \times operators are applied element-wise, $c(\mathbf{a}_j; \widehat{\mathbf{W}}_j)$ computes the cosine similarity between input \mathbf{a}_j and the rows of $\widehat{\mathbf{W}}_j$, and the hat operator scales the rows of $\widehat{\mathbf{W}}_j$ to unit norm. To see the equivalence of Eqs. (9) and (D.1), note that $\widehat{\mathbf{W}}_j \mathbf{a}_j$ computes the scalar product between each row of $\widehat{\mathbf{W}}_j$ and \mathbf{a}_j , which includes a cosine factor. We account for this by reducing the exponent to $B-1$ in Eq. (9); for a derivation, see supplement (Sec. D). Finally, note that for $B > 1$ the layer transform \mathbf{l}_j^* is *non-linear*. As a result, a non-linearity ϕ is not required for a B-cos network to model non-linear relationships.

The above discussion readily generalises to convolutional neural networks (CNNs): in CNNs, we replace the linear transforms computed by the convolutional kernels by B-cos, see Alg. 1 in supplement. Further, although we assumed a plain multi-layer network without add-ons such as skip connections, we show in Sec. 5 that the benefits of B-cos also transfer to more advanced architectures (Sec. 3.3).

3.2.1 Computing explanations for B-cos networks

As can be seen by rewriting Eq. (9), a B-cos layer effectively computes an input-dependent linear transform:

$$\mathbf{l}_j^*(\mathbf{a}_j; \mathbf{W}_j) = \widetilde{\mathbf{W}}_j(\mathbf{a}_j) \mathbf{a}_j, \quad (10)$$

$$\text{with } \widetilde{\mathbf{W}}_j(\mathbf{a}_j) = |c(\mathbf{a}_j; \widehat{\mathbf{W}}_j)|^{B-1} \odot \widehat{\mathbf{W}}_j. \quad (11)$$

Here, \odot scales the rows of the matrix to its right by the scalar entries of the vector to its left. Hence, the output of a B-cos network, see Eq. (8), is effectively calculated as

$$\mathbf{f}^*(\mathbf{x}; \theta) = \widetilde{\mathbf{W}}_L(\mathbf{a}_L) \widetilde{\mathbf{W}}_{L-1}(\mathbf{a}_{L-1}) \dots \widetilde{\mathbf{W}}_1(\mathbf{a}_1 = \mathbf{x}) \mathbf{x}. \quad (12)$$

As multiple linear transforms in sequence can be collapsed to a single one, the output $\mathbf{f}^*(\mathbf{x}; \theta)$ can be written as

$$\mathbf{f}^*(\mathbf{x}; \theta) = \mathbf{W}_{1 \rightarrow L}(\mathbf{x}) \mathbf{x}, \quad (13)$$

$$\text{with } \mathbf{W}_{1 \rightarrow L}(\mathbf{x}) = \prod_{j=1}^L \widetilde{\mathbf{W}}_j(\mathbf{a}_j). \quad (14)$$

Thus, $\mathbf{W}_{1 \rightarrow L}(\mathbf{x})$ faithfully summarises the network computations (Eq. (8)) by a single linear transform (Eq. (13)).

To explain an activation (e.g., the class logit), we can now either directly visualise the corresponding row in $\mathbf{W}_{1 \rightarrow L}$, see Figs. 1 and 10, or the *contributions* according to $\mathbf{W}_{1 \rightarrow L}$ coming from individual input dimensions. We use the resulting spatial **contributions maps** to quantitatively evaluate the explanations. In detail, the input contributions $s_j^l(\mathbf{x})$ to neuron j in layer l for an input \mathbf{x} are given by

$$s_j^l(\mathbf{x}) = [\mathbf{W}_{1 \rightarrow l}(\mathbf{x})]_j^T \odot \mathbf{x}, \quad (15)$$

with $[\mathbf{W}_{1 \rightarrow l}]_j$ denoting the j th row in matrix $\mathbf{W}_{1 \rightarrow l}$; as such, the contribution from a single pixel location (x, y) is given by $\sum_c [s_j^l(\mathbf{x})]_{(x,y,c)}$ with c the color channels.

3.2.2 Optimising B-cos networks for classification

In the following, we discuss why the linear transforms $\mathbf{W}_{1 \rightarrow L}$ (see Eq. (13)) can be expected to be interpretable, i.e., to align with relevant input patterns.

For this, first note that the output of each neuron—and thus of each layer—is bounded, cf. Eqs. (4) and (9). Since the output of a B-cos network is computed as a sequence of such bounded transforms, see Eq. (12), the output of the network as a whole is also bounded. Secondly, note that a B-cos network as a whole can only achieve its upper bound for a given input if the units in each layer achieve their upper bound. Importantly, as discussed in Sec. 3.1 (Eq. (4)),

the individual units, in turn, can only achieve their maxima by aligning with their inputs. Hence, optimising a B-cos network to maximise its output over a set of inputs will optimise the model weights to align with those inputs.

In order to take advantage of this when optimising for classification, we train the B-cos networks with the binary cross entropy (BCE) loss

$$\mathcal{L}(\mathbf{x}_i, \mathbf{y}_i) = \text{BCE}(\sigma(\mathbf{f}^*(\mathbf{x}_i; \theta) + \mathbf{b}), \mathbf{y}_i), \quad (16)$$

for input \mathbf{x}_i and its corresponding one-hot encoded class label \mathbf{y}_i . Here, σ denotes the sigmoid function, \mathbf{b} a bias, and θ the model parameters. In particular, we choose the BCE loss because it directly entails output maximisation. Specifically, in order to reduce the BCE loss, the network is optimised to maximise the (negative) class logit for the correct (incorrect) classes. As discussed in the previous paragraph, this will optimise the weights in each layer of the network to align with their inputs. In particular, they will need to align with class-specific input patterns such that these result in large outputs for the respective class logits.

Finally, note that increasing B allows to specifically reduce the output of badly aligned weights in each layer (cf. Eq. (4)). This will decrease the layer’s output strength and thus the output of the network as a whole for badly aligned weights, which increases the alignment pressure during optimisation (thus, higher $B \rightarrow$ higher alignment).

3.2.3 MaxOut to increase modelling capacity

As discussed in Sec. 3.2, a deep B-cos network with $B > 1$ does not *require* a non-linearity between subsequent layers to model non-linear relationships. This, of course, does not mean that it could not *benefit* from it. While there are many potential non-linearities to choose from, in this work, we specifically explore the option of combining the B-cos transform with the MaxOut [12] operation. In particular, we model every neuron in a B-cos network by 2 B-cos transforms¹ of which the maximal activation is forwarded:

$$\text{MaxOut}(\mathbf{x}) = \max_{i \in \{1,2\}} \{\text{B-cos}(\mathbf{x}; \mathbf{w}_i)\}. \quad (17)$$

We do so for two reasons. First, in order to forward a large signal, one such MaxOut unit still needs to have at least one weight vector that highly aligns with a given input and the alignment pressure is thus maintained during optimisation. Secondly, while the latter is also true for the ReLU [25] operation, we noticed that networks with the MaxOut operation were much easier to optimise. This could be due to the ‘dying neuron’ problem, cf. [12], and could potentially be remedied by better initialisation schemes.

3.3. Advanced B-cos networks

To test the generality of our approach, we evaluate how integrating the B-cos transform into commonly used DNN

¹Initial experiments showed no added benefit when using more than 2 units.

architectures affects their classification performance and interpretability. In order to ‘convert’ such models to B-cos networks we proceed as follows. First, every convolutional kernel / fully connected layer is replaced by the corresponding B-cos version with two MaxOut units (see Sec. 3.2.3). Secondly, any other non-linearities (e.g., ReLU, MaxPool, etc.), as well as any batch norm layers are removed to maintain the alignment pressure and to ensure that the model can be summarised via a single linear transform.

4. Experimental setting

Datasets. We evaluate the accuracies of several B-cos networks on the CIFAR-10 [19] and the ImageNet [9] datasets. We use the same datasets for the qualitative and quantitative evaluations of the model-inherent explanations.

Models. For the CIFAR10 experiments, we develop a simple fully-convolutional B-cos DNN, consisting of 9 convolutional layers, each with a kernel size of 3, followed by a global pooling operation. We evaluate a network without additional non-linearities as well as with MaxOut units, see Sec. 3.2.3. For the ImageNet experiments, we rely on the publicly available [26] implementations of the VGG-11 [35], ResNet-34 [13], InceptionNet (v3) [40], and DenseNet-121 [14] model architectures. We adapt those architectures to B-cos networks as described in Sec. 3.3. For details on the training procedure, see supplement (Sec. C).

Image encoding. We add three additional channels and encode images as $[r, g, b, 1-r, 1-g, 1-b]$, with $r, g, b \in [0, 1]$ the red, green, and blue color channels. On the one hand, this reduces a bias towards bright regions in the image² [6]. On the other hand, colors with the *same angle in the original encoding*—i.e., $[r_1, g_1, b_1] \propto [r_2, g_2, b_2]$ —are *unambiguously encoded by their angles under the new encoding*. Therefore, the linear transformation $\mathbf{W}_{1 \rightarrow l}$ can be decoded into colors just based on the angles of each pixel, see Fig. 1. For a detailed discussion, see supplement (Sec. D).

Evaluating explanations. To compare explanations for the model decisions and evaluate their faithfulness, we employ the *grid pointing game* [6]. That means we evaluate the trained models on a synthetic 3x3 grid of images of different classes and for each of the corresponding class logits measure how much positive attribution an explanation method assigns to the correct location in the grid; for a visualisation of a 2x2 grid, see Fig. 3. Following [6], we construct 500 image grids from the most confidently and correctly classified images. We compare the model-inherent contribution maps, see Eq. (15), against several commonly employed post-hoc explanation methods under two settings. First, we evaluate all methods on the B-cos networks to investigate which method provides the best explanation *for the same*

²The network is trained to maximise its output, which is bounded by the input norm. In the conventional encoding, however, black pixels, e.g., have a norm of zero and thus cannot contribute to the class logits.

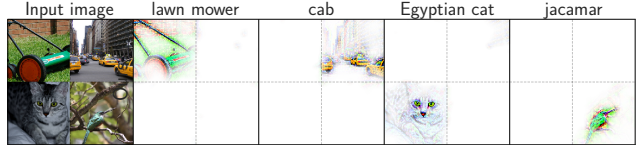


Fig. 3. 2×2 example for the pointing game. **Column 1:** input image. **Columns 2 – 5:** explanations for individual class logits.

model. Secondly, we further evaluate the post-hoc methods on pre-trained versions of the original models (VGG, ResNet, DenseNet, InceptionNet). This allows to compare explanations *between different models* and to assess the *explainability gain* obtained by converting conventional models to B-cos networks. Lastly, all non-perturbation-based attribution maps are smoothed by a 15×15 (3×3) kernel to better account for negative attributions in the localisation metric for ImageNet (CIFAR-10) images, which is negligible with respect to the overall image size.

Visualisations details. For generating the visualisations of the linear transforms for individual neurons n in layer l (cf. Figs. 1 and 10), we proceed as follows. First, we select all pixel locations (x, y) that positively contribute to the respective activation (e.g., class logit) as computed by Eq. (15); i.e., $\{(x, y) \text{ s.t. } \sum_c [\mathbf{s}_n^l(\mathbf{x})]_{(x,y,c)} > 0\}$ with c the 6 color channels (see image encoding). Then, we normalise the weights of each color channel such that the corresponding weights (e.g., for r and $1-r$) sum to 1. Note that this normalisation maintains the angle for each color channel pair (i.e., r and $1-r$), but produces values in the allowed range $r, g, b \in [0, 1]$. These normalised weights can then directly be visualised as color images. The opacity of a pixel is set to $\min(\|\mathbf{w}_{(x,y)}\|_2 / p_{99.5}, 1)$, with $p_{99.5}$ the 99.5th percentile over the weight norms $\|\mathbf{w}_{(x,y)}\|_2$ across all (x, y) .

5. Results

In this section, we analyse the performance and interpretability of B-cos networks. For this, in Sec. 5.1 we show results of ‘simple’ B-cos networks without advanced architectural elements such as skip connections or inception modules. In this context, we investigate how the B parameter influences B-cos networks in terms of performance and interpretability. Thereafter, in Sec. 5.2, we present quantitative results of the *advanced* B-cos networks, i.e., B-cos networks based on common DNN architectures (Sec. 3.3). Finally, in Sec. 5.2.1, we present and qualitatively discuss explanations for outputs of individual neurons.

5.1. Simple B-cos networks

In the following, we discuss the experimental results of simple B-cos networks evaluated on the CIFAR-10 dataset.

Accuracy. In Tab. 1, we present the test accuracies of various B-cos networks trained on CIFAR-10. We show that a plain B-cos network ($B=2$) without any add-ons (ReLU,

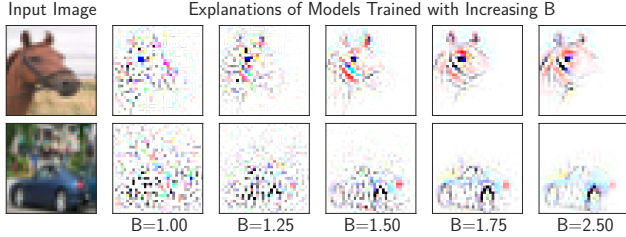


Fig. 4. Col. 1: Input images. Cols. 2-6: Explanations for classes ‘horse’ and ‘car’ of models trained with increasing values of B. With higher B, the linear transforms $\mathbf{W}_{1 \rightarrow l}$ increasingly align with discriminative patterns and thus become more interpretable.

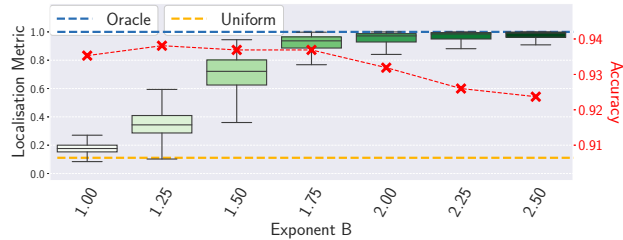


Fig. 5. Accuracy (crosses) and localisation (box plots) results for a B-cos network trained with different B values. While decreasing accuracy, a higher B yields significant gains in localisation.

	MaxOut B-cos networks								
	plain	2.00	1.00	1.25	1.50	1.75	2.00	2.25	2.50
Accuracy (%)	91.5	93.5	93.8	93.7	93.7	93.2	92.6	92.4	92.4

Tab. 1. CIFAR-10. Model accuracy of a B-cos network without any additional non-linearity (**plain**) and for B-cos networks with MaxOut (Sec. 3.2.3) and increasing values for B (left to right).

batch norm, etc.) can achieve competitive³ performance. By modelling each neuron via 2 MaxOut units (Sec. 3.2.3), the performance can be increased and the resulting model (B=2) performs on par with a ResNet-56 (achieving 93.0%, see [13]). Further, we see that an increase in the parameter B leads to a decline in performance from 93.8% for B=1.25 to 92.4% for B=2.5. Notably, despite its simple design, our strongest model with B=1.25 performs similarly to the strongest ResNet model (93.6%) reported in [13].

Model interpretability. As discussed in Sec. 3.2.2, we expect an increase in B to increase the alignment pressure on the weights during optimisation and thus influence the models’ optima, similar to the single unit case in Fig. 2. This is indeed what we observe. For example, in Fig. 4, we visualise $[\mathbf{W}_{1 \rightarrow l}(\mathbf{x}_i)]_{y_i}$ (see Eq. (13)) for different samples i from the CIFAR-10 test set. For higher values of B, the weight alignment increases notably from piece-wise linear models (B=1) to B-cos networks with higher B (B=2.5). Importantly, this does not only lead to an increase in the visual quality of the explanations, but also to quantifiable gains in model interpretability. In particular, as we show in Fig. 5, the spatial contribution maps defined by $\mathbf{W}_{1 \rightarrow l}(\mathbf{x}_i)$ (see Eq. (15)) of models with larger B values score significantly

³A ResNet-20 achieves 91.2% [13] under the same data augmentation.

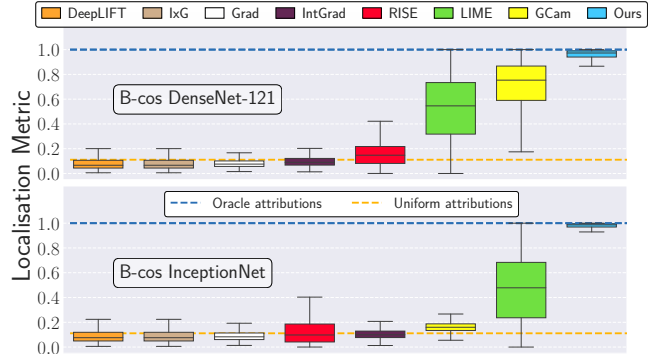


Fig. 6. Localisation results of model-inherent contribution maps (‘Ours’), Eq. (15), and post-hoc methods. For more results (VGG-11, ResNet-34, pretrained baselines), see supplement (Sec. B).

cantly higher in the localisation metric (see Sec. 4).

5.2. Advanced B-cos networks

In this section, we first quantitatively evaluate the performance and interpretability of the advanced B-cos networks, see Secs. 3.3 and 4. Then, we qualitatively investigate the interpretability of the B-cos networks in more detail.

VGG-11		ResNet-34		DenseNet-121		InceptionNet	
pre	B-cos	pre	B-cos	pre	B-cos	pre	B-cos
69.0	69.6	73.3	71.7	74.4	73.3	77.3	75.4
$\Delta = +0.6$		$\Delta = -1.6$		$\Delta = -1.1$		$\Delta = -1.9$	
B-cos DenseNet-121 training⁺						74.4 ($\Delta = 0.0$)	

Tab. 2. ImageNet. Top-1 accuracy (%) for various conventional pre-trained models (pre) and their respective B-cos version.

Bottom row: Top-1 accuracy of a B-cos DenseNet-121 trained for more epochs and a cosine learning rate schedule (training⁺).

Classification accuracies of the pretrained [1] models and their corresponding B-cos counterparts (trained from scratch) are presented in Tab. 2. The B-cos networks (except bottom row in Tab. 2) were trained for 100 epochs with the Adam optimiser, a learning rate of $2.5e^{-4}$, a batch size of 256 and no weight decay. The learning rate was decreased by a factor of 10 after 60 epochs and we used RandAugment for data augmentation; for further details on training and evaluation, see supplement (Sec. C). We would like to highlight that these results are thus obtained ‘out of the box’, i.e., with a simple and commonly used optimisation scheme for all models. Thus, in spite of the drastic changes to the model architectures (no batch norm, no ReLU, no MaxPool), we are able to achieve competitive results: our B-cos VGG-11 outperforms its conventional counterpart and we only observe minor drops in accuracy w.r.t. the baseline models for the other networks, e.g., 1.1 p.p. for the DenseNet-121 (74.4% vs. 73.3%). By training a DenseNet-121 model for 200 epochs, a batch size of 128, learning rate warm-up and a cosine learning rate schedule, we are able to close the gap between the pretrained DenseNet-121 model and its B-cos

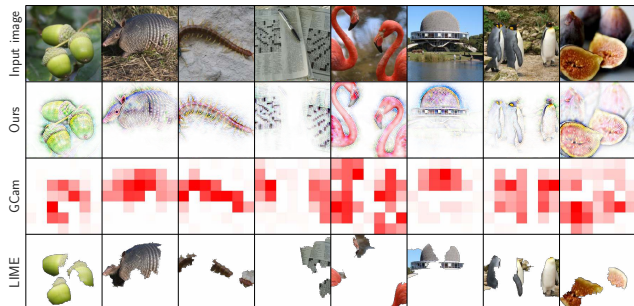


Fig. 7. Comparison between model-inherent explanations and the strongest post-hoc methods. More results in supplement (Sec. A.)

counterpart (see last row in Tab. 2, ‘training⁺’).

Model interpretability. In Fig. 6, we present the explanation quality results as assessed by the localisation metric for various post-hoc attribution methods as well as the model-inherent contribution maps (Eq. (15)). We evaluated the post-hoc methods both on the conventional pretrained models (cf. Tab. 2) as well as on their corresponding B-cos counterparts; in Fig. 6, we show results for two B-cos networks, for the remaining results we kindly refer the reader to the supplement (Sec. B). In particular, we evaluated various gradient-based methods (the ‘vanilla gradient’ (Grad) [4]; Input×Gradient (IxG), cf. [2]; Integrated Gradients (Int-Grad) [39]; DeepLIFT [33]; GradCam (GCam) [31]) and two perturbation-based methods (LIME [29], RISE [27]) for comparison. We would like to highlight the following two results. First, for all converted B-cos architectures, the model-inherent explanations not only outperform any post-hoc explanation for the models’ decisions, but achieve close to optimal scores on the localisation metric. Secondly, as we show in the supplement (Sec. B), none of the post-hoc methods that we evaluated for the conventional models provides a better explanation for those models than the linear transform $\mathbf{W}_{1 \rightarrow l}(\mathbf{x})$ provides for the B-cos networks. Hence, by using B-cos networks instead of conventional models, it is possible to drastically improve the models’ interpretability. For a qualitative comparison between the model-inherent explanations and post-hoc methods, see Fig. 7.

5.2.1 Qualitative evaluation of explanations

The following results are based on the DenseNet-121 training⁺ model, cf. Tab. 2; other advanced B-cos networks yield similar results, see supplement (Sec. A).

Every activation in a B-cos network is the result of a sequence of B-cos transforms. Hence, every neuron n in any layer l can be explained via the corresponding linear transform $[\mathbf{W}_{1 \rightarrow l}(\mathbf{x})]_n$, see Eq. (13).

For example, in Fig. 1, we visualise the linear transforms of the respective *class logits* for various input images. Given the alignment pressure during optimisation, these linear transforms align with class-discriminant patterns in the input and thus actually resemble the class objects.

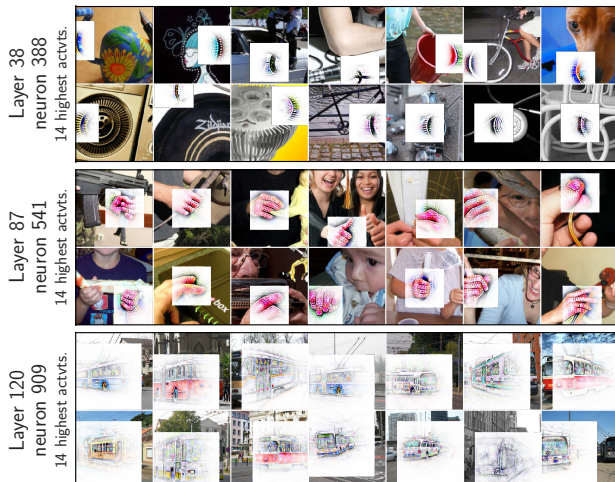


Fig. 8. Explanations for high activations of neurons from various layers. In early layers the neurons seem to encode low-level concepts (e.g., curves, see layer 38) and represent more high-level concepts in later layers (e.g., layers 87 and 120), see also Fig. 10.

Similarly, in Figs. 8 and 10, we visualise explanations for *intermediate neurons*. Specifically, in Fig. 8, we show explanations for some of the most highly activating neurons over the validation set. We find that neurons in early layers seem to represent low-level concepts (e.g., curves), and become more complex in later layers ($l=87$: hands, $l=120$: streetcars); for additional results, see supplement Sec. A.

Fig. 10 shows additional results for neurons in layer 87. We observed that some neurons become highly specific to certain concepts, such as wheels (neuron 739), faces (neuron 797), or eyes (neuron 938). These neurons do not just learn to align with simple, fixed patterns—instead, they represent semantic concepts and are robust to changes in colour, size, and pose. Further, we found that several neurons respond preferentially to watermarks, emphasising the importance of explainability for debugging DNNs: while



Fig. 9. Col. 1: Input image. Cols. 2+3: Explanations for most likely classes under the model. Col. 4: Difference of contribution maps to the two class logits, i.e., $s_{c_1}^L(\mathbf{x}) - s_{c_2}^L(\mathbf{x})$, see Eq. (15); positive values shown in orange (c_1), negative values in blue (c_2).

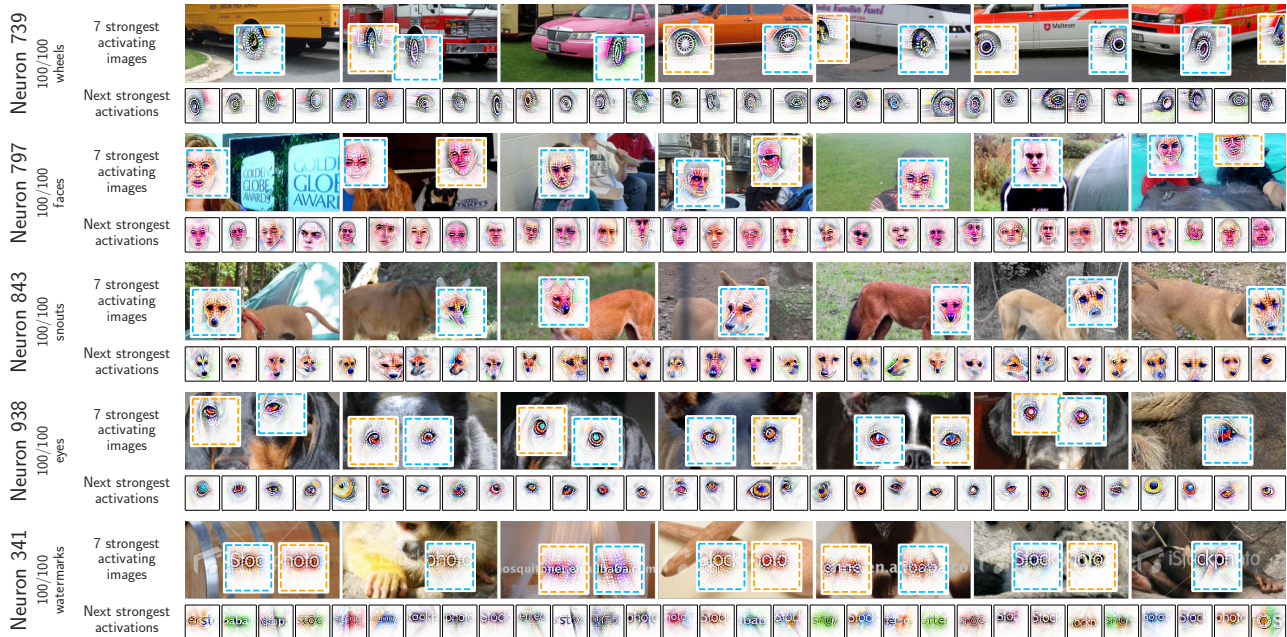


Fig. 10. Explanations of 5 individual neurons in layer 87 of a DenseNet-121. For each neuron, we provide its index number n and its concept description and specificity⁴ (left). Further, we show the 7 most activating images for each neuron (top row per neuron), in which we visualise the explanation for the highest (blue squares) activation; i.e., visualise the 72×72 center patch of the weighting $[\mathbf{W}_{1 \rightarrow i}(\mathbf{x})]_n$ for neuron n . For some images, we additionally show the explanation for the 2nd highest activation (orange squares). Lastly, we show the explanations of the highest activations (corresponding to the blue squares) for the next 30 images to highlight the neurons’ specificity.

watermarks do not seem *semantically* meaningful, they can represent an informative feature for classification if they are only present in a subset of classes, see supplement (Sec. B).

Lastly, in Fig. 9, we show explanations of the two most likely classes for images for which the model produces predictions with high uncertainty; additionally, we show the Δ -Explanation, i.e., the difference in contribution maps for the two classes, see Eq. (15). By means of the model-inherent linear mappings $\mathbf{W}_{1 \rightarrow L}$, the model can provide a human-interpretable explanation for its uncertainty: there are indeed features in each of those images that provide evidence for both of the predicted classes.

5.2.2 Limitations

By normalising the weights and computing the additional down-scaling factor (see Eq. (D.1)), the B-cos transform adds computational overhead, which we observed to increase training and inference time by up to 60% in comparison to baseline models of the same size. However, we expect this cost to decrease significantly in the future with an optimised implementation of the B-cos transform.

Moreover, in this work we specifically investigated how to integrate the B-cos transform into CNNs for image classification. How to integrate the B-cos transform into other types of architectures, such as (vision) transformers [10,42],

⁴We manually evaluated the first 100 images for each neuron and found the respective neurons to reliably highlight the assigned concept, i.e., their linear explanations $[\mathbf{W}_{1 \rightarrow 87}(\mathbf{x})]_n$ are similar to those shown in Fig. 10.

and how it affects model interpretability on other tasks and domains, remains an open question. Given the increasing dominance of transformers, we believe extending our method to such models to be an important next step.

6. Conclusion

We presented a novel approach for endowing deep neural networks with a high degree of *inherent interpretability*. In particular, we developed the B-cos transform as a modification of the linear transform to increase weight-input alignment during optimisation and showed that this can significantly increase interpretability. Importantly, the B-cos transforms can be used as a drop-in replacement for the ubiquitously used linear transforms in conventional DNNs whilst only incurring minor drops in classification accuracy. As such, our approach can increase the interpretability of a wide range of DNNs at a low cost and thus holds great potential to have a significant impact on the deep learning community. In particular, it shows that strong performance and interpretability need not be at odds. Moreover, we demonstrate that by structurally constraining *how* the neural networks are to solve an optimisation task—in the case of B-cos networks via *alignment*—allows for extracting explanations that faithfully reflect the underlying model. We believe this to be an important step on the road towards interpretable deep learning, which is an essential ingredient for building trust in DNN-based decisions, specifically in safety-critical situations.

References

- [1] Torchvision library, pretrained models. <https://pytorch.org/vision/stable/models.html>. Accessed: 2021-11-11. 6
- [2] Julius Adebayo, Justin Gilmer, Michael Muelly, Ian J. Goodfellow, Moritz Hardt, and Been Kim. Sanity Checks for Saliency Maps. In *Advances in Neural Information Processing Systems (NeurIPS)*, 2018. 1, 7, 20
- [3] Sebastian Bach, Alexander Binder, Grégoire Montavon, Frederick Klauschen, Klaus-Robert Müller, and Wojciech Samek. On Pixel-Wise Explanations for Non-Linear Classifier Decisions by Layer-Wise Relevance Propagation. *PLoS ONE*, 2015. 2
- [4] David Baehrens, Timon Schroeter, Stefan Harmeling, Motoaki Kawanabe, Katja Hansen, and Klaus-Robert Müller. How to explain individual classification decisions. *The Journal of Machine Learning Research (JMLR)*, 2010. 7, 20
- [5] Wieland Brendel and Matthias Bethge. Approximating CNNs with Bag-of-local-Features models works surprisingly well on ImageNet. In *International Conference on Learning Representations (ICLR)*, 2019. 2
- [6] Moritz Böhle, Mario Fritz, and Bernt Schiele. Convolutional Dynamic Alignment Networks for Interpretable Classifications. In *Proceedings of the IEEE Conference on Computer Vision and Pattern Recognition (CVPR)*, 2021. 2, 5, 18, 21
- [7] Chaofan Chen, Oscar Li, Daniel Tao, Alina Barnett, Cynthia Rudin, and Jonathan Su. This Looks Like That: Deep Learning for Interpretable Image Recognition. In *Advances in Neural Information Processing Systems (NeurIPS)*, 2019. 2
- [8] Subhajit Das, Panpan Xu, Zeng Dai, Alex Endert, and Liu Ren. Interpreting Deep Neural Networks through Prototype Factorization. In *International Conference on Data Mining Workshops (ICDMW)*, 2020. 2
- [9] Jia Deng, Wei Dong, Richard Socher, Li-Jia Li, Kai Li, and Li Fei-Fei. ImageNet: A large-scale hierarchical image database. In *Proceedings of the IEEE Conference on Computer Vision and Pattern Recognition (CVPR)*, 2009. 5
- [10] Alexey Dosovitskiy, Lucas Beyer, Alexander Kolesnikov, Dirk Weissenborn, Xiaohua Zhai, Thomas Unterthiner, Mostafa Dehghani, Matthias Minderer, Georg Heigold, Sylvain Gelly, Jakob Uszkoreit, and Neil Houlsby. An Image is Worth 16x16 Words: Transformers for Image Recognition at Scale. In *International Conference on Learning Representations*, 2021. 8
- [11] Kamaleddin Ghiassi-Shirazi. Generalizing the convolution operator in convolutional neural networks. *Neural Processing Letters*, 50(3):2627–2646, 2019. 2
- [12] Ian Goodfellow, David Warde-Farley, Mehdi Mirza, Aaron Courville, and Yoshua Bengio. Maxout networks. In *International Conference on Machine Learning (ICML)*, 2013. 4
- [13] Kaiming He, Xiangyu Zhang, Shaoqing Ren, and Jian Sun. Deep residual learning for image recognition. In *Proceedings of the IEEE Conference on Computer Vision and Pattern Recognition (CVPR)*, 2016. 2, 5, 6
- [14] Gao Huang, Zhuang Liu, Laurens Van Der Maaten, and Kilian Q Weinberger. Densely connected convolutional networks. In *Proceedings of the IEEE Conference on Computer Vision and Pattern Recognition (CVPR)*, 2017. 2, 5, 19
- [15] Sergey Ioffe and Christian Szegedy. Batch Normalization: Accelerating Deep Network Training by Reducing Internal Covariate Shift. In *International Conference on Machine Learning (ICML)*, 2015. 2
- [16] Beomsu Kim, Junghoon Seo, and Taegyun Jeon. Bridging Adversarial Robustness and Gradient Interpretability. *Safe Machine Learning workshop at ICLR*, 2019. 2
- [17] Been Kim, Martin Wattenberg, Justin Gilmer, Carrie J. Cai, James Wexler, Fernanda B. Viégas, and Rory Sayres. Interpretability Beyond Feature Attribution: Quantitative Testing with Concept Activation Vectors (TCAV). In *International Conference on Machine Learning (ICML)*, 2018. 2
- [18] Diederik P. Kingma and Jimmy Ba. Adam: A Method for Stochastic Optimization. In *International Conference on Learning Representations (ICLR)*, 2015. 20
- [19] Alex Krizhevsky. Learning multiple layers of features from tiny images. Technical report, University of Toronto, 2009. 2, 5
- [20] Weiyang Liu, Zhen Liu, Zhiding Yu, Bo Dai, Rongmei Lin, Yisen Wang, James M. Rehg, and Le Song. Decoupled Networks. In *Proceedings of the IEEE Conference on Computer Vision and Pattern Recognition (CVPR)*, 2018. 2
- [21] Weiyang Liu, Yan-Ming Zhang, Xingguo Li, Zhen Liu, Bo Dai, Tuo Zhao, and Le Song. Deep Hyperspherical Learning. In *Advances in Neural Information Processing Systems (NeurIPS)*, 2017. 2
- [22] Scott M. Lundberg and Su-In Lee. A Unified Approach to Interpreting Model Predictions. In *Advances in Neural Information Processing Systems (NeurIPS)*, 2017. 2
- [23] Chunjie Luo, Jianfeng Zhan, Xiaohe Xue, Lei Wang, Rui Ren, and Qiang Yang. Cosine normalization: Using cosine similarity instead of dot product in neural networks. In *International Conference on Artificial Neural Networks (ICANN)*, 2018. 2
- [24] Guido F. Montúfar, Razvan Pascanu, KyungHyun Cho, and Yoshua Bengio. On the Number of Linear Regions of Deep Neural Networks. In *Advances in Neural Information Processing Systems (NeurIPS)*, 2014. 1
- [25] Vinod Nair and Geoffrey E. Hinton. Rectified Linear Units Improve Restricted Boltzmann Machines. In *International Conference on Machine Learning (ICML)*, 2010. 1, 4
- [26] Adam Paszke, Sam Gross, Francisco Massa, Adam Lerer, James Bradbury, Gregory Chanan, Trevor Killeen, Zeming Lin, Natalia Gimelshein, Luca Antiga, Alban Desmaison, Andreas Kopf, Edward Yang, Zachary DeVito, Martin Raison, Alykhan Tejani, Sasank Chilamkurthy, Benoit Steiner, Lu Fang, Junjie Bai, and Soumith Chintala. PyTorch: An Imperative Style, High-Performance Deep Learning Library. In *Advances in Neural Information Processing Systems (NeurIPS)*, 2019. 5
- [27] Vitali Petsiuk, Abir Das, and Kate Saenko. RISE: Randomized Input Sampling for Explanation of Black-box Models. In *British Machine Vision Conference (BMVC)*, 2018. 2, 7, 12, 20

- [28] Prajit Ramachandran, Barret Zoph, and Quoc V. Le. Searching for Activation Functions. In *International Conference on Learning Representations (ICLR), Workshop*, 2018. [2](#)
- [29] Marco Tulio Ribeiro, Sameer Singh, and Carlos Guestrin. "Why Should I Trust You?": Explaining the Predictions of Any Classifier. In *International Conference on Knowledge Discovery and Data Mining (SIGKDD)*, 2016. [2](#), [7](#), [12](#), [20](#)
- [30] Wojciech Samek, Grégoire Montavon, Sebastian Lapuschkin, Christopher J. Anders, and Klaus-Robert Müller. Explaining deep neural networks and beyond: A review of methods and applications. *Proceedings of the IEEE*, 109(3):247–278, 2021. [1](#)
- [31] Ramprasaath R. Selvaraju, Michael Cogswell, Abhishek Das, Ramakrishna Vedantam, Devi Parikh, and Dhruv Batra. Grad-CAM: Visual Explanations from Deep Networks via Gradient-Based Localization. In *International Conference on Computer Vision (ICCV)*, 2017. [2](#), [7](#), [12](#), [20](#)
- [32] Harshay Shah, Prateek Jain, and Praneeth Netrapalli. Do Input Gradients Highlight Discriminative Features? *CoRR*, abs/2102.12781, 2021. [2](#)
- [33] Avanti Shrikumar, Peyton Greenside, and Anshul Kundaje. Learning Important Features Through Propagating Activation Differences. In *International Conference on Machine Learning (ICML)*, 2017. [1](#), [2](#), [7](#), [12](#), [20](#)
- [34] Karen Simonyan, Andrea Vedaldi, and Andrew Zisserman. Deep Inside Convolutional Networks: Visualising Image Classification Models and Saliency Maps. In *International Conference on Learning Representations (ICLR), Workshop*, 2014. [2](#)
- [35] Karen Simonyan and Andrew Zisserman. Very Deep Convolutional Networks for Large-Scale Image Recognition. In Yoshua Bengio and Yann LeCun, editors, *International Conference on Learning Representations (ICLR)*, 2015. [2](#), [5](#)
- [36] Jost Tobias Springenberg, Alexey Dosovitskiy, Thomas Brox, and Martin A. Riedmiller. Striving for Simplicity: The All Convolutional Net. In *International Conference on Learning Representations (ICLR), Workshop*, 2015. [2](#)
- [37] Suraj Srinivas and François Fleuret. Full-Gradient Representation for Neural Network Visualization. In *Advances in Neural Information Processing Systems (NeurIPS)*, 2019. [2](#)
- [38] Suraj Srinivas and François Fleuret. Rethinking the Role of Gradient-based Attribution Methods for Model Interpretability. In *International Conference on Learning Representations (ICLR)*, 2021. [2](#)
- [39] Mukund Sundararajan, Ankur Taly, and Qiqi Yan. Axiomatic Attribution for Deep Networks. In Doina Precup and Yee Whye Teh, editors, *International Conference on Machine Learning (ICML)*, 2017. [2](#), [7](#), [12](#), [20](#)
- [40] C. Szegedy, V. Vanhoucke, S. Ioffe, J. Shlens, and Z. Wojna. Rethinking the Inception Architecture for Computer Vision. In *Proceedings of the IEEE Conference on Computer Vision and Pattern Recognition (CVPR)*, 2016. [2](#), [5](#)
- [41] Dimitris Tsipras, Shibani Santurkar, Logan Engstrom, Alexander Turner, and Aleksander Madry. Robustness May Be at Odds with Accuracy. In *International Conference on Learning Representations (ICLR)*, 2019. [2](#)
- [42] Ashish Vaswani, Noam Shazeer, Niki Parmar, Jakob Uszkoreit, Llion Jones, Aidan N Gomez, Łukasz Kaiser, and Illia Polosukhin. Attention is all you need. *Advances in Neural Information Processing Systems (NeurIPS)*, 2017. [8](#)
- [43] Chen Wang, Jianfei Yang, Lihua Xie, and Junsong Yuan. Kervolutional neural networks. In *Proceedings of the IEEE Conference on Computer Vision and Pattern Recognition (CVPR)*, 2019. [2](#)
- [44] Mengjiao Yang and Been Kim. Benchmarking Attribution Methods with Relative Feature Importance. *CoRR*, abs/1907.09701, 2019. [1](#)
- [45] Bolei Zhou, Aditya Khosla, Àgata Lapedriza, Aude Oliva, and Antonio Torralba. Learning Deep Features for Discriminative Localization. In *Proceedings of the IEEE Conference on Computer Vision and Pattern Recognition (CVPR)*, 2016. [2](#)
- [46] Georgios Zoumpourlis, Alexandros Doumanoglou, Nicholas Vretos, and Petros Daras. Non-linear convolution filters for CNN-based learning. In *Proceedings of the IEEE Conference on Computer Vision and Pattern Recognition (CVPR)*, pages 4761–4769, 2017. [2](#)

Supplementary Material

Table of Contents

In this supplement to our work on B-cos DNNs, we provide:

(A) Additional qualitative results **12**

In this section, we show additional *qualitative* results of the model-inherent explanations. This includes visualisations for the same model explored in the main paper (DenseNet-121)—both for the class-logits and for intermediate neurons—as well as results for other B-cos networks.

Moreover, we provide additional comparisons to post-hoc importance attribution methods that were not shown in the main paper.

(B) Additional quantitative results **18**

In this section, we show additional *quantitative* results. In particular, we present the localisation metric results for two additional B-cos networks as well as those of the pre-trained conventional DNNs.

Moreover, we present ImageNet results for B-cos networks trained without any additional non-linearities (apart from the B-cos transform) and for different model sizes.

Finally, we investigate the predictive power of the watermark neurons in more detail.

(C) Implementation details **20**

In this section, we describe the model architectures, the training procedure, and the evaluation of model interpretability in more detail.

(D) Additional derivations and discussions **21**

In this section, we provide a short derivation for Eq. (3)→Eq. (9). Further, we provide a more detailed explanation of the relevance of the image encoding for visualising the linear transforms $\mathbf{W}_{1 \rightarrow l}(\mathbf{x})$.

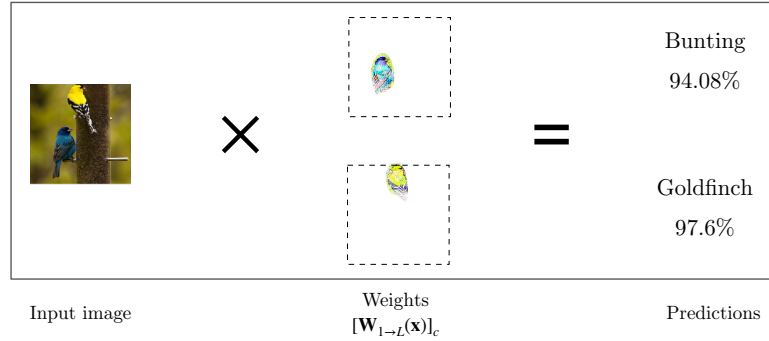


Fig. A1. Illustration of the computations of a B-cos network. For a given input image (left), the model computes an *input-dependent* linear transform $\mathbf{W}_{1 \rightarrow L}(\mathbf{x})$ (center). The scalar product between the input and the weights $[\mathbf{W}_{1 \rightarrow L}(\mathbf{x})]_c$ for class c (row c of $\mathbf{W}_{1 \rightarrow L}(\mathbf{x})$), yields the class logits for the respective class. To obtain class probabilities (right), we apply the sigmoid function. Since the B-cos networks are trained with the BCE loss, they produce probabilities *per class* and *not a probability distribution over classes*. Thus, the probabilities do not sum to 1. For illustration purposes, we only visualise the positive contributions according to $\mathbf{W}_{1 \rightarrow L}(\mathbf{x})$.

A. Additional qualitative examples

In Fig. A1, we illustrate how the linear mappings $\mathbf{W}_{1 \rightarrow L}(\mathbf{x})$ are used to compute the outputs of B-cos networks. In particular, with this we would like to highlight that these linear mappings do not only constitute qualitatively convincing visualisations. Instead, they in fact constitute the actual linear transformation matrix that the model effectively applies to the input to compute its outputs and thus constitute an accurate summary of the model computations.

A.1. Additional explanations for class logits [DenseNet-121]

Comparisons between explanation methods In Fig. A2, we show additional comparisons between the model-inherent explanations based on the linear mapping $[\mathbf{W}_{1 \rightarrow L}(\mathbf{x}_i)]_c$ and some post-hoc methods; in particular, we show results for GradCam (GCam) [31], LIME [29], Integrated Gradients (IntG) [39], DeepLIFT [33], and RISE [27] on the most confidently classified image of the first 15 classes in Fig. A3. While GCam highlights similar regions and LIME also yields explanations in color, these explanations are post-hoc approximations of model behaviour. In contrast, the model-inherent explanations are not only of higher visual quality, but also summarise the model computations for the presented classes accurately, cf. Fig. A1.

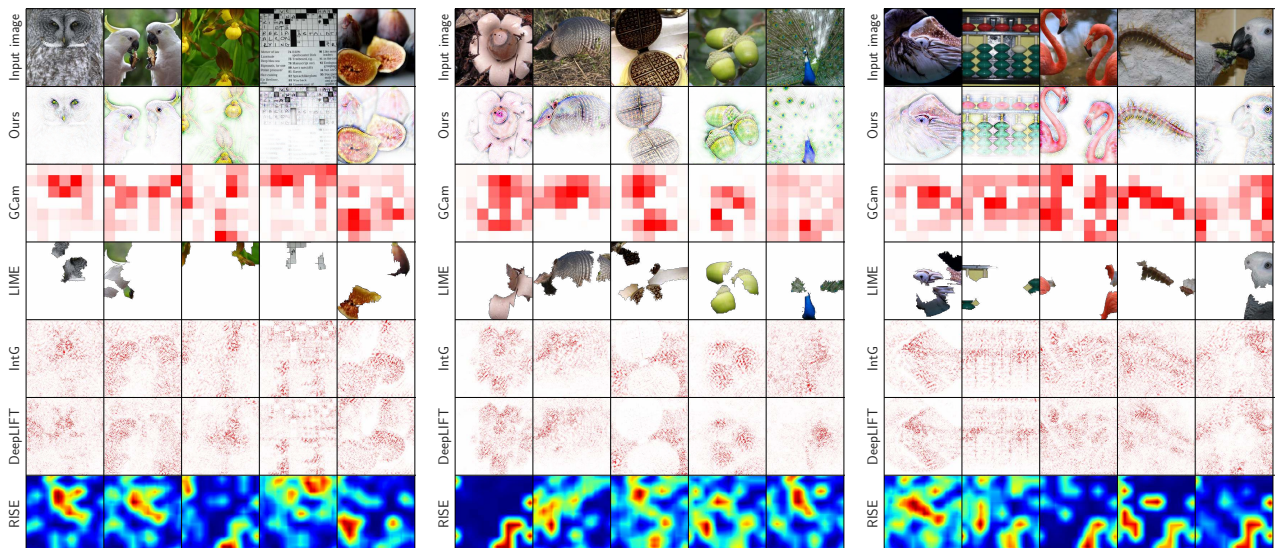


Fig. A2. Comparison between the model-inherent explanations (‘Ours’) and various post-hoc explanation methods, evaluated for the most confident image for the first 15 of the classes shown in Figs. A3 and A4. Note that for RISE we use its default colormap.

Model-inherent explanations. In Figs. A3 and A4, we present additional qualitative examples of the linear mappings $[\mathbf{W}_{1 \rightarrow L}(\mathbf{x}_i)]_c$ that explain the class logit c in the B-cos DenseNet-121 model, see Eq. (13) in the main paper. Specifically,

we show the 3 most confidently classified examples for 48 different classes; these classes were selected as those that had the highest mean confidence (sum of class logits) in the three most confidently classified images.

Note that due to the **alignment pressure** induced by the B-cos transform, the linear mappings $[\mathbf{W}_{1 \rightarrow L}(\mathbf{x}_i)]_c$ align with class-discriminative features in the input images. Interestingly, we find that these features can be highly specific to particular regions in the image (see, e.g., great grey owl, centipede, school bus, planetarium, three-toed sloth, parking meter), but can also cover the entire image and include background features that correlate with the presented classes. For the latter, see e.g., the presented examples of the gondola or the golfcart: for some of these images, the weight matrix also aligns with *context features* in the background. Note, however, that the model has never been explicitly trained to highlight only the respective class objects and it is therefore expected to find that context features are also used by the model to increase its output score for the respective classes.

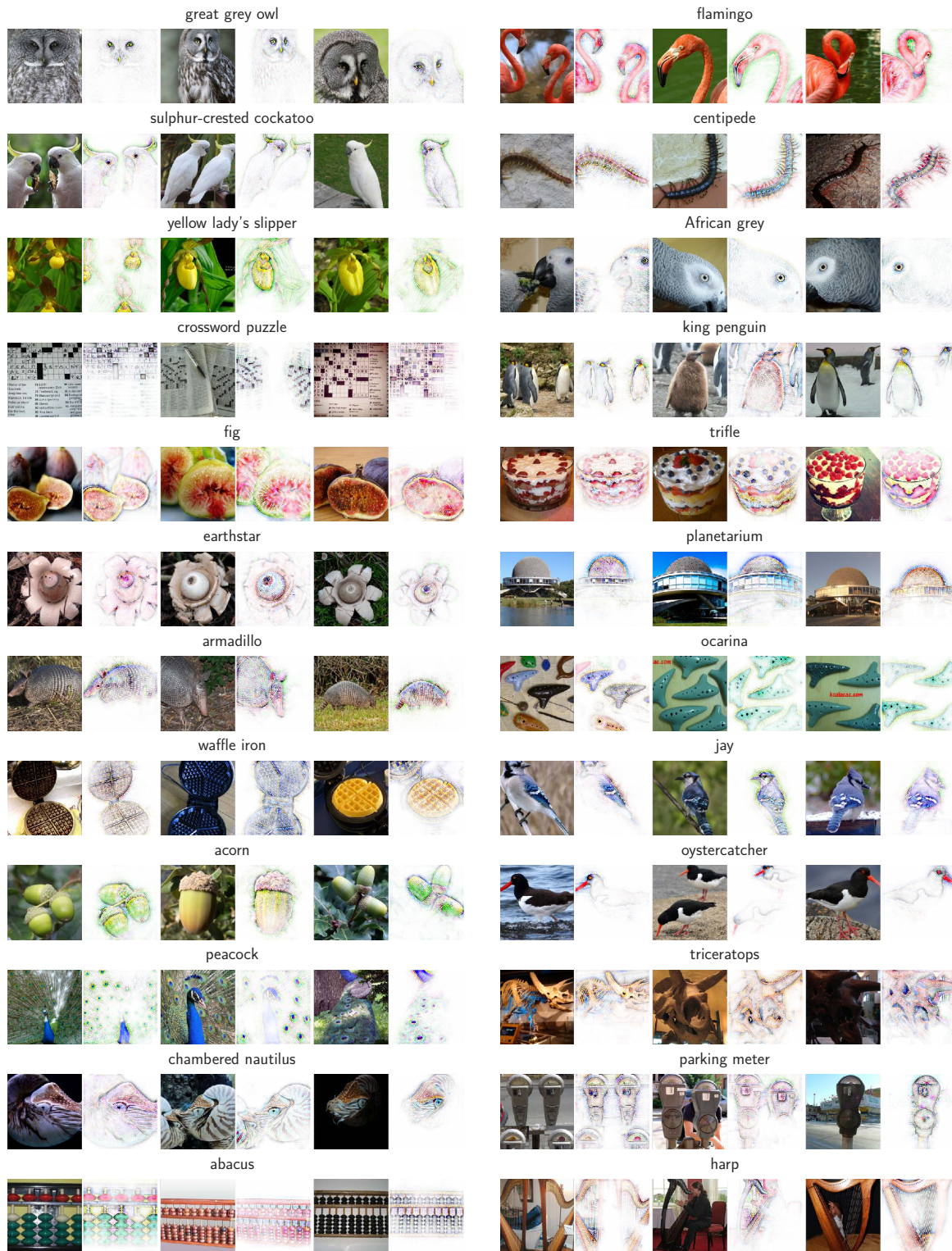


Fig. A3. First three samples \mathbf{x}_i^c and linear mappings $[\mathbf{W}_{1 \rightarrow L}(\mathbf{x}_i^c)]_c$ for 24 of the most confidently classified classes c from the Imagenet dataset. Specifically, the classes are sorted by the sum of the logits for those three samples. Left: Classes 1-12. Right: Classes 13-24.

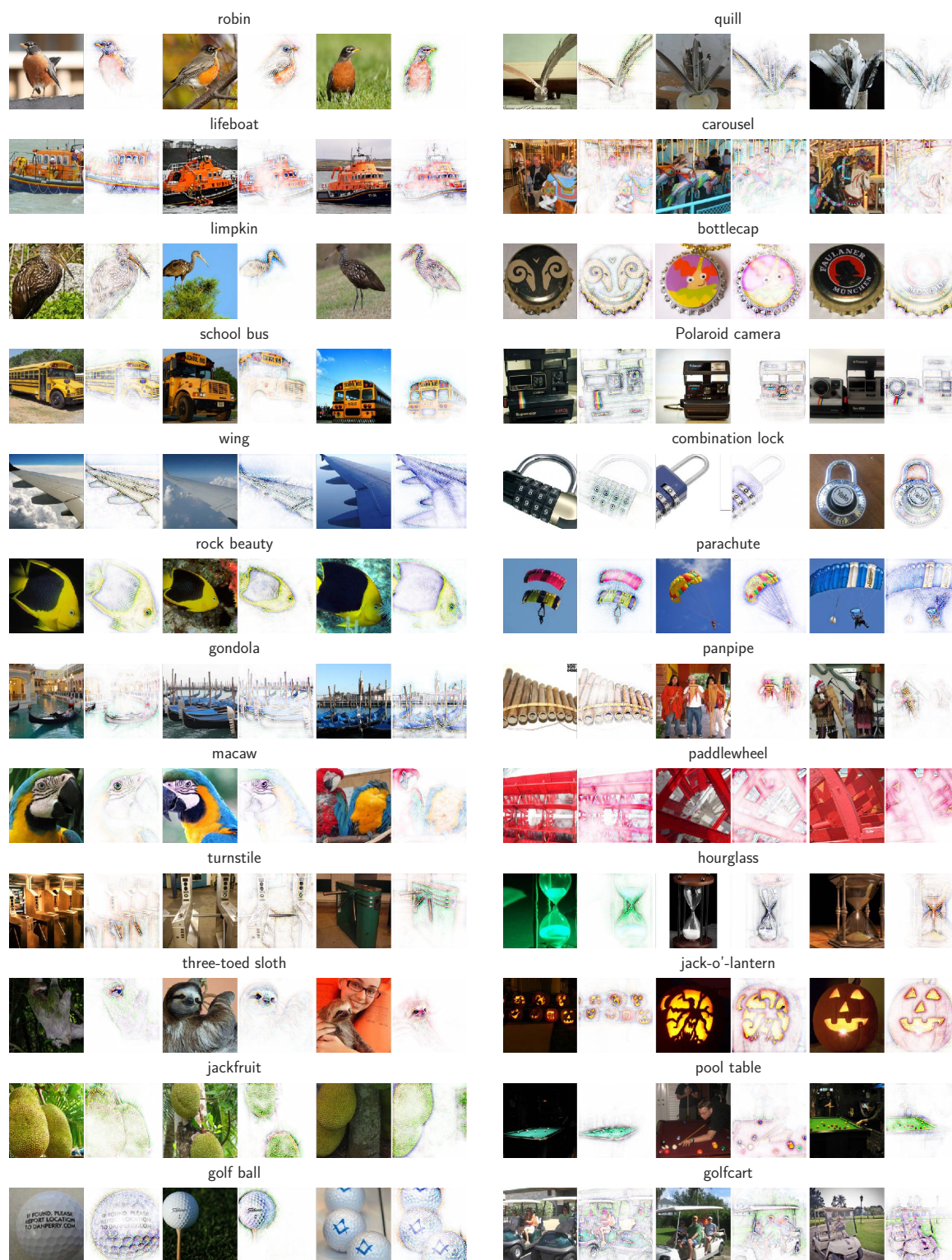


Fig. A4. First three samples \mathbf{x}_i^c and linear mappings $[\mathbf{W}_{1 \rightarrow L}(\mathbf{x}_i^c)]_c$ for 24 of the most confidently classified classes c from the Imagenet dataset. Specifically, the classes are sorted by the sum of the logits for those three samples. Left: Classes 25-36. Right: Classes 37-48.

A.2. Additional explanations for intermediate neurons [DenseNet-121]

In Fig. A5, we present additional qualitative examples of the linear mappings $[\mathbf{W}_{1 \rightarrow l}(\mathbf{x}_i)]_n$ that explain the activations of intermediate neurons n in layer $l=87$. Specifically, we show 16 out of the 20 most highly activating neurons and their explanations, which were not already shown in the main paper. We find that all neurons seem to represent specific concepts, such as faces, snouts, water, grass, etc.



Fig. A5. Additional examples of some of the 20 most highly activating neurons in layer 87 of the B-cos DenseNet-121 model. Similar to the results shown in the main paper, we observe the neurons to represent highly specific concepts.

A.3. Explanations for other B-cos networks

In Fig. A6, we show explanations for neurons in intermediate layers of a B-cos ResNet-34, a B-cos InceptionNet, and a B-cos VGG-11. We observe that the complexity of the neurons tends to increase, similarly to the neurons in the B-cos DenseNet-121 model.



Fig. A6. Explanations for intermediate neurons for other B-cos networks. In particular, we show results for B-cos ResNet-34 (a), B-cos VGG-11 (b), and B-cos InceptionNet (c); cf. Tab. 2 in the main paper. Similarly to the DenseNet-121 model, we observe the linear mappings $[\mathbf{W}_{1 \rightarrow l}]_n$ to be of high visual quality and increase in complexity throughout the layers for all networks.

B. Additional quantitative evaluations

B.1. Localisation scores.

In Figs. B1 and B2, we present the localisation results of the *grid pointing game* [6].

In particular, in Fig. B1, we show that of all methods, the best explanation for the B-cos network is given by the model-inherent linear transforms $\mathbf{W}_{1 \rightarrow L}(\mathbf{x})$ (Eq. 13, main paper).

Moreover, from Fig. B2, we can estimate the *interpretability gain* due to replacing the linear transform in conventional models by the B-cos transform: specifically, we see that no method explains the baseline models better than the model-inherent linear transforms explain the respective B-cos network.

We note that LIME and GCam often achieve good localisation scores. However, we would like to highlight the low reliability of those explanations (high variance). Further, LIME requires many forward passes through the model to estimate feature importance, whereas the model-inherent explanations of B-cos models can be extracted in a single forward and backward pass. GCam, on the other hand, only provides explanations with comparably low resolution (cf. also Fig. A2), since it only explains the model’s classification head. As such, it does not actually explain the full model, but only a small fraction of it (e.g., 1 out of 121 layers for DenseNet-121). In contrast, the model-inherent explanations of the B-cos networks provide high-resolution explanations *in color* and explain the entire model.

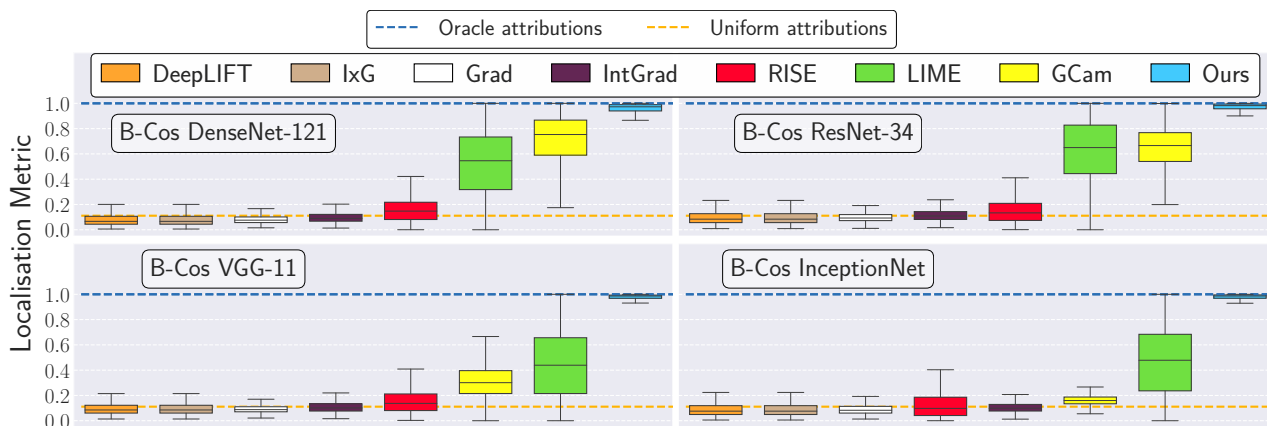


Fig. B1. Localisation metric results for all attribution methods for the converted B-cos models. Note that the DenseNet-121 and Inception-Net results are the same as in the main paper in Fig. 5.

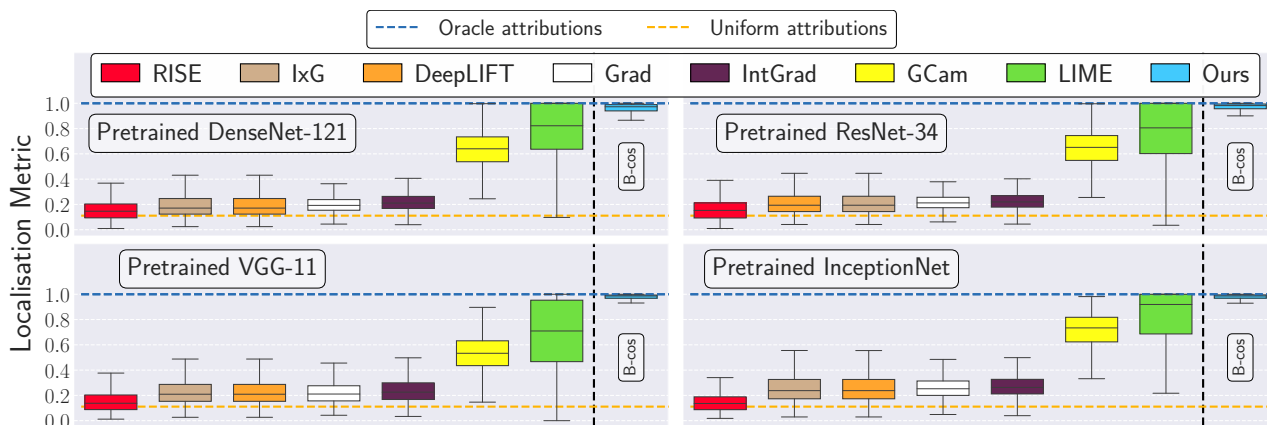


Fig. B2. Results of the localisation metric for all post-hoc attribution methods for the original, pre-trained models. Additionally, we show the B-cos results of the converted models as a reference; note that the equivalent to ‘Ours’ in piece-wise linear models is given by ‘IxG’.

B.2. Impact of model size on performance

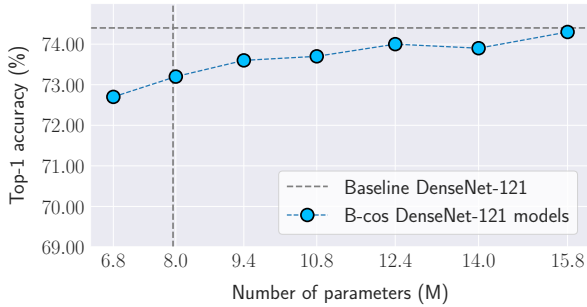


Fig. B3. Top-1 accuracy on ImageNet of B-cos DenseNet-121 models of different sizes (i.e., *growth factors*, see [14]). These models were trained with 2 MaxOut units. For reference, we indicate the number of parameters and the accuracy results of a conventional DenseNet-121 model (Baseline, dashed lines).

MaxOut	B-cos DenseNet-121 models							
	no	Maxout with 2 units						
g-factor	32	20	22	24	26	28	30	32
#Params. (M)	7.9	6.8	8.0	9.4	10.8	12.4	14.0	15.8
Accuracy (%)	72.6	72.8	73.2	73.6	73.7	74.0	73.9	74.3

Standard DenseNet-121: accuracy 74.4; parameters 7.9; g-factor 32

Tab. B1. Top-1 accuracies (%) on ImageNet of B-cos DenseNet-121 models with different growth factors (g-factors), see [14], and with and without MaxOut. Note that the B-cos DenseNet-121 model without MaxOut does not employ any non-linearities other than B-cos. Results of a standard DenseNet-121 model shown for reference.

In Fig. B3 and Tab. B1, we present the results of two ablation studies. On the one hand, we show the results for a B-cos DenseNet-121 model trained without MaxOut, which therefore has a similar number of parameters as the baseline model (a few less due to not using BatchNorm nor biases). On the other hand, we evaluate DenseNet models with two MaxOut units per neuron of different sizes. For this, we modify the *growth factor* of the model architectures, see [14].

In particular, in Tab. B1, we show that despite not employing any non-linearity apart from the B-cos transform, the model with no MaxOut units also achieves competitive performance (left-most column in Tab. B1). Specifically, we only observe a minor drop in performance with respect to a conventional DenseNet-121 model ($74.4 \rightarrow 72.6$, $\Delta=1.8$).

Further, the accuracy of B-cos networks improves with model size; note that the B-cos DenseNet-121 with a growth factor of 22 and 2 MaxOut units has a similar size to the pretrained baseline DenseNet-121 model. While there is a drop in performance ($74.4 \rightarrow 73.2$, $\Delta=1.2$), the B-cos version still shows competitive accuracy results. Lastly, note that increasing model size via maxout is computationally more efficient than just increasing the growth factor in a model with a single unit, as the number of feature channels remains unchanged.

B.3. Class-discriminative information content in watermark neurons

As discussed in the main paper, we observed that some neurons seem to specifically respond to watermarks in images. While this might not seem like a semantically meaningful feature, we find that the distribution of watermarks is in fact highly skewed. In particular, in Fig. B4, we plot the distribution of classes among the images corresponding to the 500 highest neuron activations of the ‘watermark neuron’ (index 341); we manually inspected those images and found that neuron 341 consistently activated on text within or overlayed over the images. These images clearly exhibit a non-uniform class distribution, indicating that watermarks indeed represent a highly informative feature for the classification task.

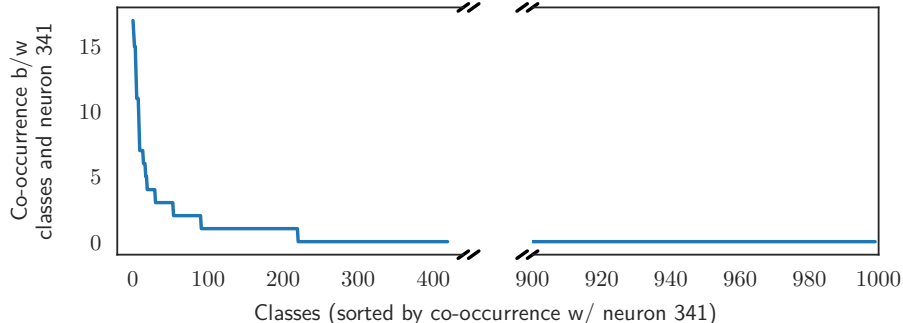


Fig. B4. Class distribution among the images corresponding to the 500 highest activations of the watermark neuron (341). The co-occurrence distribution between classes and watermarks is indeed highly skewed and only a fraction of all classes is represented among these images. This indicates high discriminative power of the watermark for classification.

C. Implementation details

Here, we provide implementation details regarding implementation of a convolutional B-cos transform (Alg. 1), the training procedure (C.1) and the *post-hoc* attribution methods (C.2).

Alg. 1: Pseudocode for B-cos-Conv2d, cf. Eq. (9) in the main paper.

```
1 #  $\mathbf{x}$ : input,  $\widehat{\mathbf{W}}$ : normed weights,  $k$ : kernel size,  $d_f$ : index of feature dimension
2 def bcov2d(x,  $\widehat{\mathbf{W}}$ , k, B):
3     linear_out = conv2d(x,  $\widehat{\mathbf{W}}$ ) # =  $\widehat{\mathbf{W}}\mathbf{x}$ 
4     norm = sumpool2d(x.pow(2).sum( $d_f$ ), k).sqrt()
5     cos = linear_out / norm.unsqueeze( $d_f$ )
6     scaling = cos.abs().pow(B-1) # =  $|c(\mathbf{x}; \widehat{\mathbf{W}})|^{B-1}$ 
7     return scaling * linear_out # =  $|c(\mathbf{x}; \widehat{\mathbf{W}})|^{B-1}\widehat{\mathbf{W}}\mathbf{x}$ 
```

C.1. Training and evaluation procedure

C.1.1 CIFAR10

Architecture. For our CIFAR10 experiments, we used a 9-layer architecture with the following specifications: kernel size $k = [3, 3, 3, 3, 3, 3, 3, 3, 1]$, stride $s = [1, 1, 2, 1, 1, 2, 1, 1, 1]$, padding $p = [1, 1, 1, 1, 1, 1, 1, 1, 0]$, and output channels $o = [64, 64, 128, 128, 128, 256, 256, 256, 10]$ for layers $l = [1, 2, 3, 4, 5, 6, 7, 8, 9]$ respectively.

When increasing the parameter B, we observed the input signal to decay strongly over the network layers, which resulted in zero outputs and hindered training. To overcome this, we scaled all layer outputs with a fixed scalar γ , which we set such that $\log_{10} \gamma = 1.5 \times B - 1.75$, which improved signal propagation. To counteract the artificial upscaling of the signal at the network output, we divided the network output by a fixed constant T for each B, such that $\log_{10} T = [-3, -3, -2, 1, 2, 2, 3]$ for $B = [1, 1.25, 1.5, 1.75, 2, 2.25, 2.5]$ respectively. In future work, we aim to examine how to automatically set an optimal scale for a given network in more detail.

Training. We trained our CIFAR10 models for 100 epochs with Adam [18], an initial learning rate of 1×10^{-3} , and a batch size of 64. Further, we used a cosine learning rate schedule and decayed the learning rate to 1×10^{-5} over the 100 epochs and applied horizontal flipping and padded random cropping for augmenting the data. We used a bias term of $\mathbf{b} = \log(0.1/0.9)$, which yields a uniform probability distribution for zero inputs ($[\mathbf{f}(\mathbf{x} = \mathbf{0})]_i = [\sigma(\mathbf{W}_{1 \rightarrow L} \mathbf{0} + \mathbf{b})]_i = 0.1 \forall i$).

C.1.2 ImageNet

Training. Similar to the CIFAR10 experiments, we observed signals to decay quickly for deep networks and to be dependent on the number of channels used. To overcome this, we scaled the layer outputs by $\gamma = s/\sqrt{d}$ with s a network-dependent hyperparameter and d the input dimensionality (i.e., k^2c for a convolutional layer with kernel size k and an input with c feature channels). Specifically, we chose $s = 100$ for DenseNets and ResNets, $s = 200$ for the InceptionNet, and $s = 1000$ for the VGG model.

Moreover, as in the CIFAR10 experiments, we divided the network outputs by a temperature parameter T . In detail, for the results in this paper we set $\log_{10} T = -3$ for the DenseNet models, $\log_{10} T = 1$ for ResNet, $\log_{10} T = 0$ for InceptionNet, and $\log_{10} T = -1$ for the VGG model. These parameters were experimentally determined to achieve good accuracies and stable training behaviour. In future work, we plan to investigate how to set the temperature parameter automatically.

Finally, we added the auxiliary loss in the InceptionNet with a weighting of $\lambda = 1$, used images of size $s = 299$ for Inception (224 otherwise), and employed RandAugment with $n = 2$ and $m = 9$. The bias term \mathbf{b} was set to $\mathbf{b} = \log(0.01/0.99)$ for all ImageNet experiments.

C.2. Attribution methods

We compare the model-inherent explanations, given by the linear transform $\mathbf{W}_{1 \rightarrow L}(\mathbf{x})$, against the following post-hoc attribution methods: the vanilla gradient (Grad, [4]), ‘Input×Gradient’ (IxG, cf. [2]), Integrated Gradients (IntGrad, [39]), DeepLIFT ([33]), GradCam (GCam, [31]), LIME ([29]), and (RISE [27]).

For all methods except RISE, LIME, and GCam, we rely on the captum library (github.com/pytorch/captum). For IntGrad, we set $n_steps = 50$ for integrating over the gradients. For RISE and LIME, we used the official implementations

available at github.com/eclique/RISE and github.com/marotcr/lime respectively. We generated 500 masks for RISE and set the hyperparameters s and p to their default values of $s = 8$ and $p = 0.1$. Similarly, we used 500 samples for LIME, and used the default values for the kernel size ($k = 4$) and the number of features ($n = 5$).

C.2.1 Localisation metric

We evaluated all attribution methods on the *grid pointing game* [6]. For this, we constructed 500 3×3 grid images. For an example of a 2×2 grid, see Fig. 3 in the main paper. As was done in [6], we sorted the images according to the models’ classification confidence for each class and then sampled a random set of classes for each multi-image. For each of the sampled classes, we then included the most confidently classified image in the grid that had not already been used in a previous grid image.

D. Additional derivations and discussions

D.1. On the B-cos transform in matrix form

In the following, we provide additional details on how to express the B-cos transform in matrix form.

As shown in Eq. (3) in the main paper, the B-cos transform is given by

$$\text{B-cos}(\mathbf{x}; \mathbf{w}) = \|\widehat{\mathbf{w}}\| \|\mathbf{x}\| \times |c(\mathbf{x}, \widehat{\mathbf{w}})|^B \times \text{sgn}(c(\mathbf{x}, \widehat{\mathbf{w}})), \quad (\text{D.1})$$

$$\text{with } c(\mathbf{x}, \mathbf{w}) = \cos(\angle(\mathbf{x}, \mathbf{w})), \quad (\text{D.2})$$

$$\widehat{\mathbf{w}} = \mathbf{w} / \|\mathbf{w}\|, \quad (\text{D.3})$$

$\angle(\mathbf{x}, \mathbf{w})$ returning the angle between \mathbf{x} and \mathbf{w} , and sgn the sign function. Note that the sign function can be expressed as $\text{sgn}(a) = a/|a|$ for $|a| \neq 0$ and zero otherwise. Hence, Eq. (D.1) can be expressed as

$$\text{B-cos}(\mathbf{x}; \mathbf{w}) = \|\widehat{\mathbf{w}}\| \|\mathbf{x}\| \times |c(\mathbf{x}, \widehat{\mathbf{w}})|^B \times \text{sgn}(c(\mathbf{x}, \widehat{\mathbf{w}})) \quad (\text{D.4})$$

$$\text{(replace sgn)} \quad = \|\widehat{\mathbf{w}}\| \|\mathbf{x}\| \times |c(\mathbf{x}, \widehat{\mathbf{w}})|^B \times c(\mathbf{x}, \widehat{\mathbf{w}}) / |c(\mathbf{x}, \widehat{\mathbf{w}})| \quad (\text{D.5})$$

$$\text{(combine cos terms)} \quad = \|\widehat{\mathbf{w}}\| \|\mathbf{x}\| \times |c(\mathbf{x}, \widehat{\mathbf{w}})|^{B-1} \times c(\mathbf{x}, \widehat{\mathbf{w}}) \quad (\text{D.6})$$

$$\text{(reorder)} \quad = \|\widehat{\mathbf{w}}\| \|\mathbf{x}\| \times c(\mathbf{x}, \widehat{\mathbf{w}}) \times |c(\mathbf{x}, \widehat{\mathbf{w}})|^{B-1} \quad (\text{D.7})$$

$$\text{(write first three factors as linear transform)} \quad = \widehat{\mathbf{w}}^T \mathbf{x} \times |c(\mathbf{x}, \widehat{\mathbf{w}})|^{B-1}. \quad (\text{D.8})$$

For clarity, we marked the changes between lines in the above equations in red.

From Eq. (D.8) it becomes clear that a B-cos transform simply computes a rescaled linear transform. Thus, multiple units in parallel (i.e., a layer \mathbf{I}^* of B-cos units) can easily be expressed in matrix form via

$$\mathbf{I}^*(\mathbf{x}) = |c(\mathbf{x}, \widehat{\mathbf{W}})|^{B-1} \times \widehat{\mathbf{W}} \mathbf{x}. \quad (\text{D.9})$$

Here, the \times , \cos , and absolute value operators are applied element-wise and the rows of $\widehat{\mathbf{W}}$ are given by $\widehat{\mathbf{w}}_n$ of the individual units n .

Hence, the output of each unit (entry in output vector \mathbf{I}^*) is the down-scaled linear transform from Eq. (D.8). Note that Eq. (D.9) is the same as Eq. (9) in the main paper.

D.2. On the relevance of image encoding for the visualisations

As we describe in the main paper, we encode image pixels as $[r, g, b, 1-r, 1-g, 1-b]$. This has two important advantages.

On the one hand, as argued by [6], this overcomes a bias towards bright pixels. For this, note that the model output is computed as a linear transform of the input \mathbf{x} . As such, the contribution to the output per pixel is given by the weighted input strength. In particular, a specific pixel location (i, j) with color channels c contributes $\sum_c w_{(i,j,c)} x_{(i,j,c)}$ to the output. Under the conventional encoding—i.e., $[r, g, b]$ —, a black pixel is encoded by $x_{(i,j,c)} = 0$ for $c \in \{1, 2, 3\}$ and can therefore not contribute to the model output. Since we train the model to maximise its outputs (binary cross entropy loss, see Sec. 3.2.2 in the main paper), the network will preferentially encode bright pixels, as these can produce higher contributions for maximising the output than dark pixels. In contrast, under the new encoding dark and bright pixels have the same amount of ‘signal’ that can be weighted, i.e., $\sum_c x_{(i,j,c)} = 3 \forall (i, j)$.

Moreover, this encoding allows to unambiguously infer the color of a pixel solely based on the angle of the pixel vector $[r, g, b, 1-r, 1-g, 1-b]$. To contrast this with the original encoding, consider a pixel that is (almost) completely black and given by $[r, g, b]$ with $g=0, b=0, r=0.001$. This pixel has the same angle as a red pixel, given by $r=1, g=0, b=0$. Thus, these two colors cannot be disambiguated based on their angle. By adding the three additional color channels $[1-r, 1-g, 1-b]$, each color channel is uniquely encoded by the direction of the color channel vector, e.g., $[r, 1-r]$. Finally, note that the B-cos transform induces an alignment pressure on the weights, i.e., the model weights are optimised such that $\mathbf{W}_{1 \rightarrow L}$ points in the same direction as (important features in) the input. Consequently, the weights will reproduce the *angles* of the pixels, but there is no constraint on their *norm*. Since the angle is sufficient for inferring the color, we can nevertheless decode the angles of the weight vectors into RGB colors, as, e.g., shown in Figs. [A2](#), [A3](#), [A4](#), [A5](#) and [A6](#).